Research on the Identification Mechanism of Coal Gangue Based on the Differences of Mineral Components

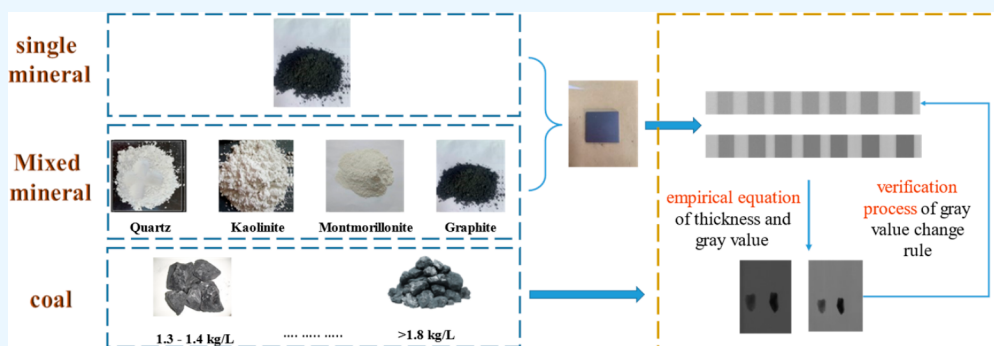Chenguang Yang, Jianqiang Yin,* Liqin Wu, Qiuyu Zeng, and Liwei Zhang

Read Online

ACCESS | Metrics & More | Article Recommendations

ABSTRACT: For coal and gangue, intelligent sorting processes for separation, the use of coal and gangue mineral components with different fundamental differences, and the study of different properties of minerals and coal with different scales and density regarding the gray value change law are presented. The results show that the gray value of single minerals and mixed minerals gradually decreases with the increase of their thickness and density. The greater the density of minerals, the smaller the gray value at the same thickness, and the same rule applies to different coal ranks. Via regression analysis methods, the values of the regression equation parameter *a* of pure minerals for graphite, quartz, kaolinite, and montmorillonite are 59.25, 65.69, 61.61, and 58.02 in the high-energy region, respectively. In the low-energy region, they are 174.95, 177.31, 186.95, and 161.81. For the regression equation parameter of mixed minerals in the form of two mixed minerals (graphite and quartz, kaolinite, or montmorillonite) and three kinds of mineral mixing (graphite−kaolinite and quartz; graphite−montmorillonite and quartz; graphite−kaolinite and montmorillonite), the gray values are 151.12, 156.00, 153.13,152.43, 152.98, and 151.98 in the high-energy region, respectively; in the low-energy region, they are 193.34, 201.34, 192.93, 191.26, 194.68, and 193.08. The phenomenon for the gray range of two kinds of single minerals locates in the range of mixed minerals that was formed from a single mineral observed after the regression equation of mixed mineral was verified by a single mineral, which agrees with the X-ray recognition pattern. In the end, as the density of coking coal, fat coal, and gas coal increases, the gray value decreases, which was in agreement with single- and mixed-mineral analyses.

1. INTRODUCTION

Coal is one of the most important energy sources in China and occupies a very important position compared to other energy sources.[1,2] As there is a large amount of gangue mixed with raw coal as an accompaniment in the coal mining process, coal gangue separation is crucial.[3,4]

Intelligent photoelectric sorting technology, which has been rapidly developed in the coal sorting industry in recent years, has the advantages of high speed, high accuracy, modularity and integrated scalability,[5−9] low operating cost and energy consumption, easy operation and maintenance, and no water consumption compared with traditional coal sorting methods. Singh et al.[10] proposed a new separation of ore particles (Mn, Fe, and Al_2O_3) based on the visual texture and a radial-based neural network method, which extracts texture features from a large number of ore images and trains them with a neural network to

finally achieve ore separation. Li et al.[11] extracted the texture information from coal gangue images by using the method of grayscale cogeneration matrix, which improved the accuracy of visible light separation of coal gangue. Alfarzaeai et al.[12] established a new coal gangue recognition model (CGR-CNN) based on a convolutional neural network (CNN), which used thermal imaging of coal gangue as the separation feature. The model provides 100% accuracy for coal recognition, 97.5% accuracy for gangue recognition, and 98.75% overall
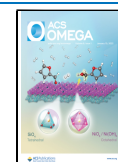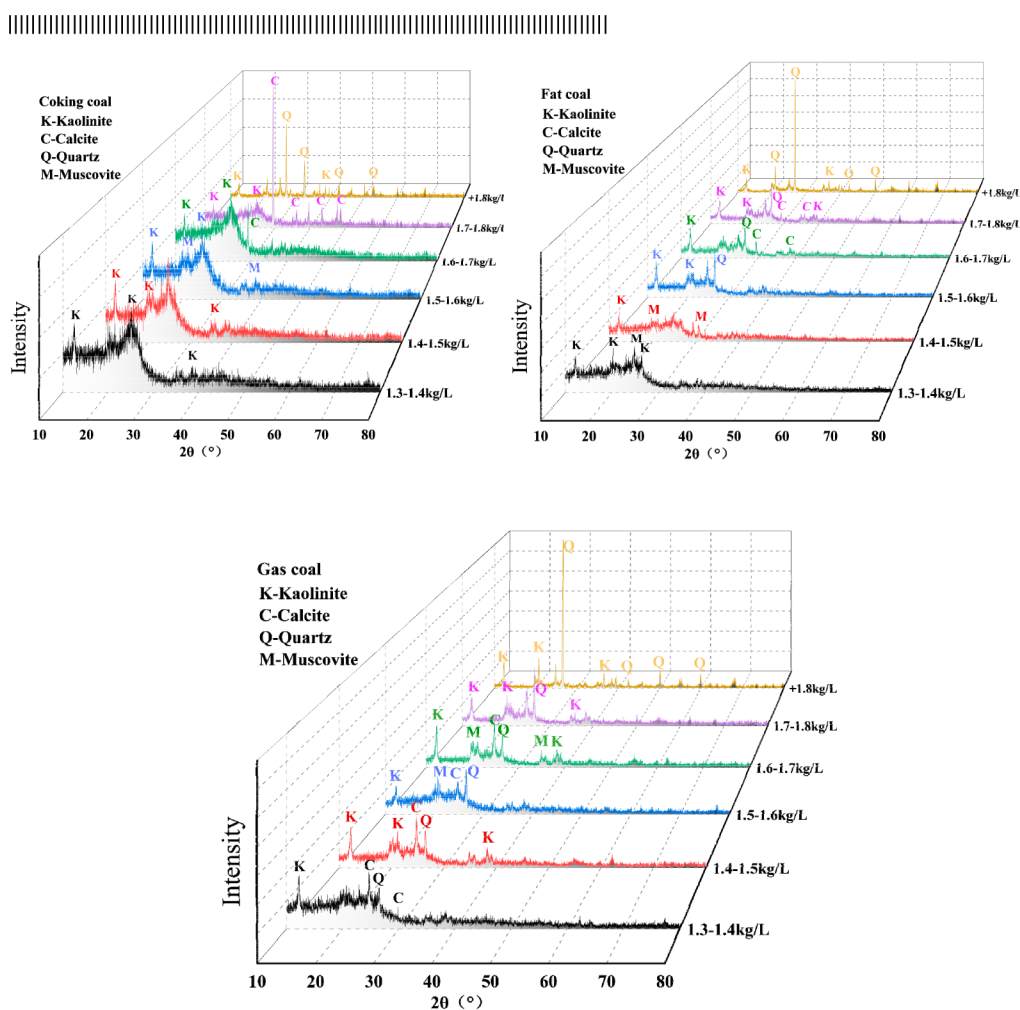
Figure 1. XRD analysis of coking coal, gas coal, and fat coal.

prediction accuracy. Eshaq et al.[13] used a support vector machine to train the grayscale information on the infrared image of coal gangue, and the accuracy of this method for gangue recognition is 97.83%. Dou et al.[14] employed the relief-SVM method to find optimal features and develop the best classifiers; moreover, it was validated through the experiments considering two mining areas, wherein the mean accuracy was 95.5−97.0% and 94.0−98.0%. Guo et al.[15] proposed a recognition method by considering differences in the dielectric properties of coal gangue and combined it with a support vector machine (SVM); the results were accurate, and the method was efficient.

According to the above analysis, it can be determined that the research on the intelligent sorting of coal gangue focuses on finding the image features of coal gangue under visible light, which is mainly reflected in the optimization of the training model and the diversification of image features.[16−20] There is less research on this fundamental difference between coal and gangue mineral components. To further develop the photoelectric separation technology of coal and gangue, the impact of thickness and density of single and mixed minerals on the gray value was studied via the regression equation of the gray value.[21−25]

2. EXPERIMENTAL PROCEDURE

2.1. Materials. In this study, three different types of test samples of coal, single minerals, and mixed minerals were utilized.

First, the coals used in the experiments were coking, gas, and fat coals from the Huainan mine in China. The moisture content was 1.26%, 1.63%, and 2.02%, respectively, and the coal samples were divided into three size classes of 30−50, 50−100, and 30−100 mm after sieving, and then each size class was divided into six density classes of 1.3−1.4, 1.4−1.5, 1.5−1.6, 1.6−1.7, 1.7−1.8, and >1.8 kg/L after float and sink tests.

Second, samples of single minerals were made based on the mineral composition of coal. A Shimadzu LabX XRD-6000 X-ray diffractometer was used for XRD analysis of the crushed raw coal. The measured particle size of each coal type was 30−100 mm, and the test was performed by a step scanning method, with scanning angle range of 10−80°, scanning speed of 5 deg/min, step length of 0.02°, emitter tube Cu target, tube intensity signal of 40 kV, and current of 30 mA. The X-ray pattern of the raw coal was qualitatively analyzed by MDI Jade 6.5 software to determine its main mineral composition. The results are shown in Figure 1.

The results show that the main clay mineral components in coal are quartz, kaolinite, and montmorillonite. Next, organic carbon was replaced by graphite and samples of single minerals were prepared. The graphite, quartz, kaolinite, and montmor-

Table 1. Properties of Samples

sample	particle size (μm)	crystal formula	molecular weight (g/mol)
graphite	13	C	12
quartz	65	SiO_2	60
montmorillonite	39	$(Na,Ca)_{0.33}(Al,Mg)_2[Si_4O_{10}](OH)_2 \cdot nH_2O$	682
kaolinite	39	$Al_2O_3 \cdot 2SiO_2 \cdot 2H_2O$	258

Table 2. Preparation of Mixed Minerals[a]

| sample	project	sample parameters					
G:K, G:Q and G:M	quality ratio	6:1	5:1	4:1	3:1	2:1	1:1
	total quality (g)	10.5	10.8	11.2	12	13.5	18
	total thickness (mm)	3	3.1	3.2	3.5	4	5.5
G:K:Q, G:M:Q and G:K:M	quality ratio	6:1:1	5:1:1	4:1:1	3:1:1	2:1:1	1:1:1
	total quality (g)	12	12.6	13.5	15	18	27
	total thickness (mm)	3.6	3.8	4	4.2	5.5	9
G:Q:M:K	quality ratio	6:1:1:1	5:1:1:1	4:1:1:1	3:1:1:1	2:1:1:1	1:1:1:1
	total quality (g)	13	14.4	15.75	18	22.5	36
	total thickness (mm)	3.5	3.8	4.5	5.5	7	11.8

[a]G stands for graphite, K stands for kaolinite, M stands for montmorillonite, and Q stands for quartz

illonite were all obtained from Shanghai Aladdin Biochemical Technology (China). The purity grade of these samples was above 99.8%, and the water content was below 0.01%; the details of each material are shown in Table 1.

Then the four kinds of minerals were pressed into block samples with thickness of 4.0, 4.5, 5.0, 6.0, 6.5, and 7.0 mm.

Finally, the four pure minerals were mixed in the same proportion and pressed into block samples of different thickness, and the amount of graphite in the mixed minerals was used as the variable, as shown in Table 2.

2.2. System. The test device is mainly composed of X-ray generator, ray receiver, belt, and computer as shown in Figure 2.
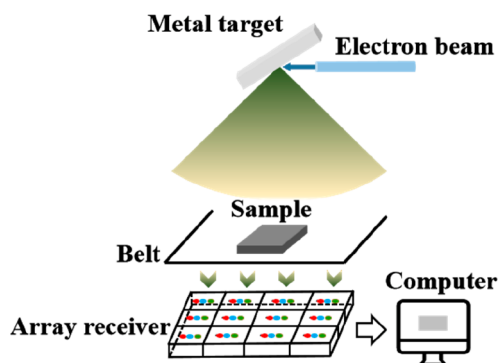

Figure 2. Schematic of the experimental system.

First, in the process of testing, the photoelectric effect and Compton−Debye effect occur when X-rays pass through the sample. This process does not take into account the electron pair effect for X-ray intensity did not reach 1.02 MeV.[26−28] X-ray intensity decreases at the same time as photons were absorbed and reflected via electrons inside atoms of the sample. Next, the attenuated X-ray was converted into an image signal using a photoelectric detector. Since the system has a high-energy region and a low-energy region, two images are obtained for one sample.[29,30]

Different kinds of coal samples and pure minerals of the main mineral components in coal are used for the test samples. The attenuation pattern of X-rays is determined for coal samples of different density and particle size. Furthermore, the effect of mineral composition in coal on the ash value is determined by the X-ray attenuation law of a single mineral.[31,32]

3. RESULTS AND DISCUSSION

The graphite, quartz, montmorillonite, and kaolinite specimens are put on the belt separately. Then the attenuated ray signals were accepted by the X-ray receiver and converted into digital signals. Two images of high and low energy were formed for each sample, as shown in Figure 3, and the images were processed using MATLAB to count the grayscale peaks.
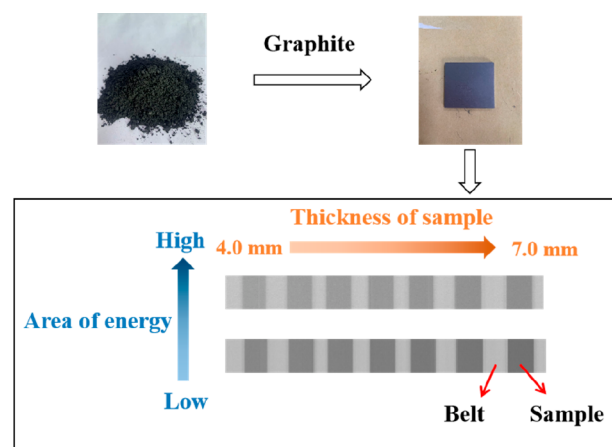
Figure 3. Grayscale image of the sample.

3.1. Single Mineral. After filtering and noise reduction of the grayscale map of a single-mineral sample, the grayscale value of the target region of the image was extracted, and the result is shown in Figure 4.

From the gray values of single mineral samples, we can determine that the gray values of single minerals decrease with increasing thickness and the gray value in the thickness range of 4−5 mm shows faster descent than that of 5−7 mm. The relationship was more consistent with the empirical formula of the index. At the same thickness, the main trends of the gray values of the four single minerals are graphite > kaolinite >
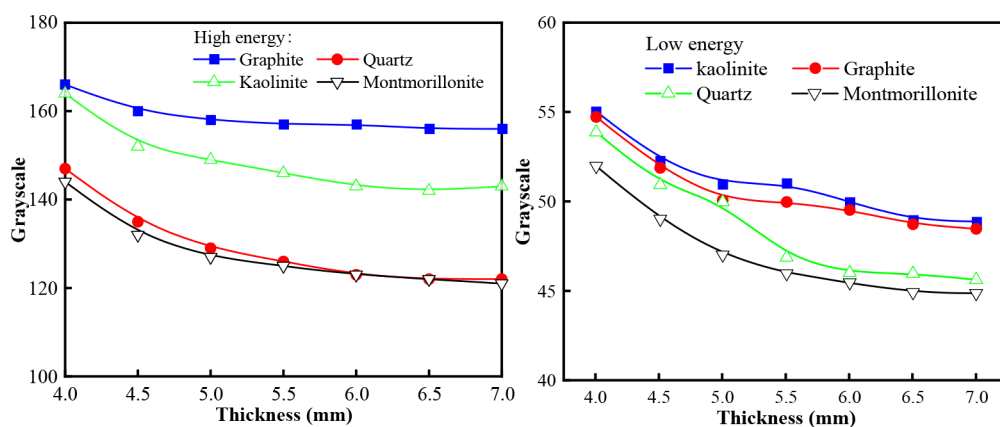
Figure 4. Relationship between mineral composition, thickness, and gray peak value.

Table 3. Regression Equation of Gray Value of Single Mineral

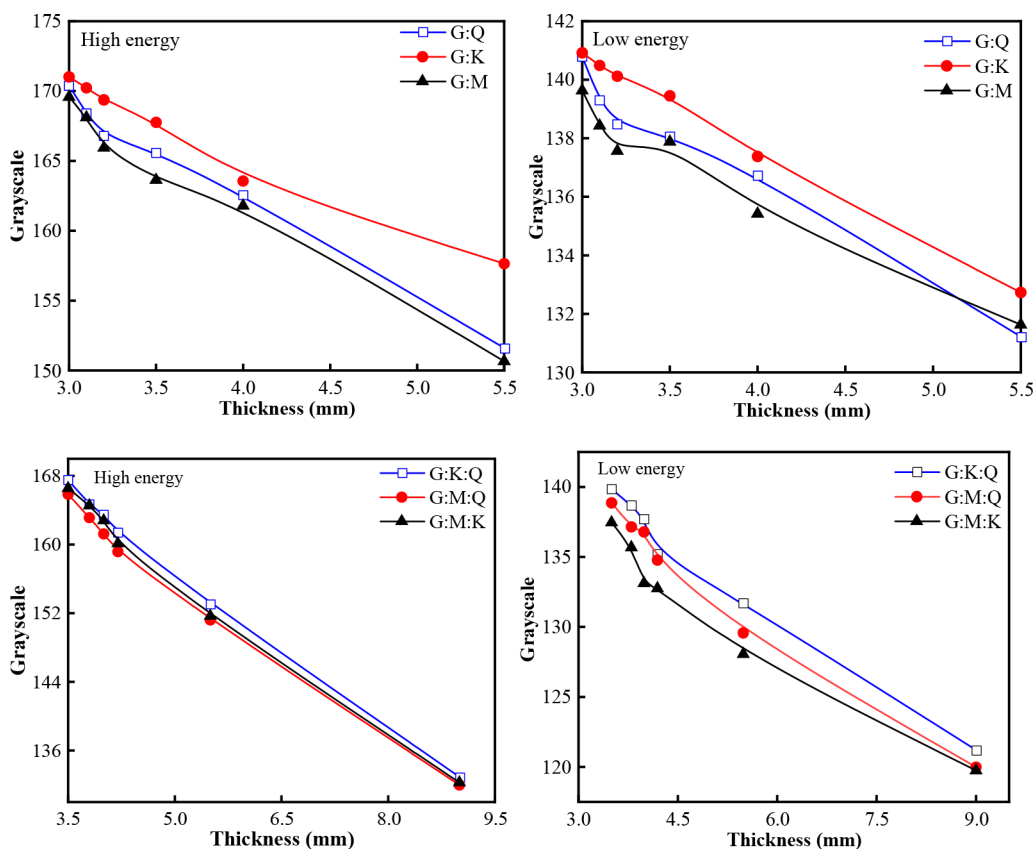| sample	regression equation		correlation factor	
	low energy	high energy	low energy	high energy
graphite	$y = 174.95e^{-0.0168x}$	$y = 59.25e^{-0.0279x}$	−0.9614	−0.9595
quartz	$y = 177.31e^{-0.0580x}$	$y = 65.69e^{-0.0552x}$	−0.9606	−0.9660
kaolinite	$y = 186.95e^{-0.0422x}$	$y = 61.61e^{-0.0342x}$	−0.9529	−0.8627
montmorillonite	$y = 161.80e^{-0.0426x}$	$y = 58.02e^{-0.0373x}$	−0.8799	−0.8745

Figure 5. Gray value of mixed minerals.

quartz > montmorillonite, compared with their density performance in the natural state (graphite < kaolinite < quartz < montmorillonite); therefore, the greater the density of different minerals, the smaller the gray value.

With the mineral thickness as the independent variable x and the grayscale value as the dependent variable y, an empirical equation $y = a \cdot e^{bx}$ (a and b are regression coefficients) was used to fit the thickness−grayscale peak numerical model for a single mineral, as shown in Table 3.

The lowest absolute value of the correlation coefficient of the numerical model in the table is 0.8627, indicating that there is a good correlation between the thickness of graphite, quartz,

Table 4. Regression Equation of Gray Value of Mixed Minerals

| sample	regression equation		correlation factor	
	low energy	high energy	low energy	high energy
G:Q	$y' = 193.34e^{-0.0441x'}$	$y' = 151.12e^{-0.0256x'}$	−0.994 9	−0.988 8
G:K	$y'y' = 201.34e^{-0.0534x'}$	$y' = 156.00e^{-0.0331x'}$	−0.996 8	−0.993 9
G:M	$y' = 192.93e^{-0.0412x'}$	$y' = 153.13e^{-0.0275x'}$	−0.995 7	−0.994 5
G:M:Q	$y' = 191.26e^{-0.0405x'}$	$y' = 152.43e^{-0.0266x'}$	−0.996 7	−0.995 9
G:K:Q	$y' = 194.68e^{-0.0438x'}$	$y' = 152.98e^{-0.0274x'}$	−0.992 9	−0.992 6
G:M:K	$y' = 193.08e^{-0.0432x'}$	$y' = 151.98e^{-0.0263x'}$	−0.996 9	−0.995 1
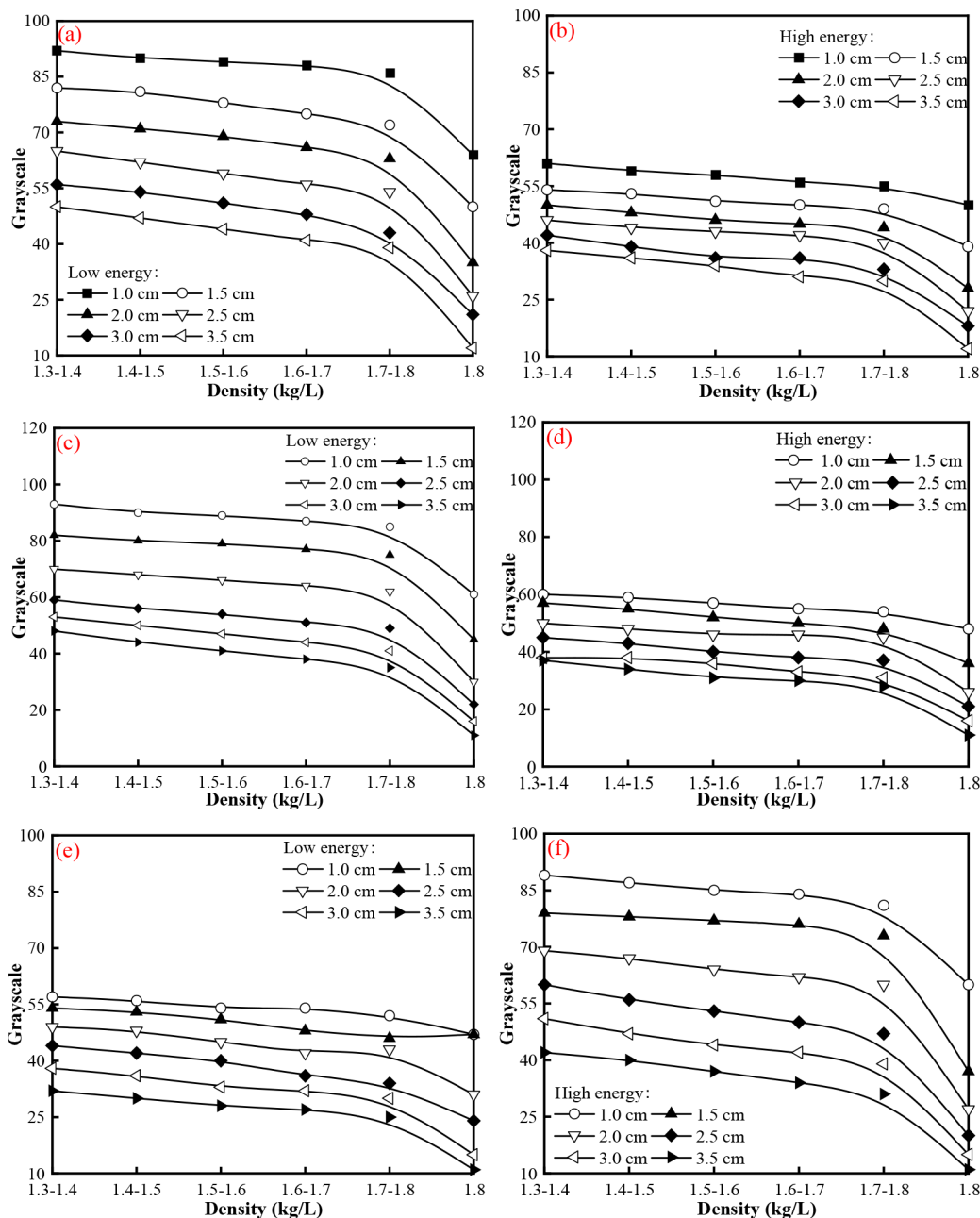
Figure 6. (a−f) Relationship between density and gray value of different coal types.

kaolinite, and montmorillonite and the gray value, and this relationship is not affected by mineral type.

3.2. Mixed Mineral. The grayscale values of the mixed mineral samples are shown in Figure 5.

According to the gray values of mixed-mineral samples, the gray value of the same mixed minerals decreases with the increase of thickness. At the same thickness, the mixed-mineral gray value of graphite and montmorillonite is the smallest, while the mixed-mineral gray value of graphite and kaolinite is the
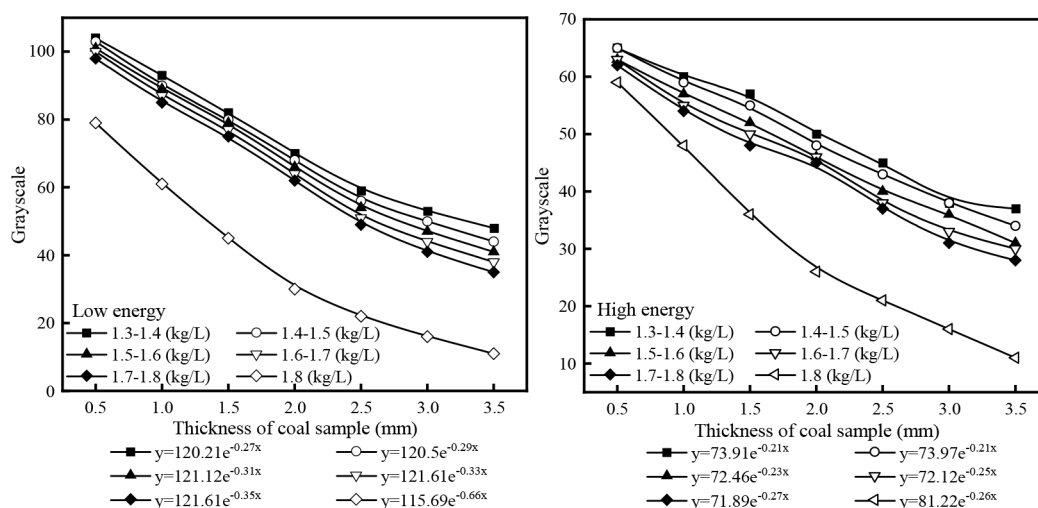
Figure 7. Gray value attenuation model of fat coal.

largest. At the same density, the mineral content gradually becomes larger with the increase of thickness, and when less attenuated rays are received by the detector after X-ray transmission through the minerals, the lower the gray value of the pictures converted by the computer and calculated by MATLAB. In the test, montmorillonite has the highest density, and the mixed mineral of graphite and montmorillonite has the highest density at the same thickness, resulting in the smallest gray value, which is consistent with the conclusion of the single pure mineral gray value test.

By analyzing the pure minerals, it was found that the gray peak value was in the form of exponential variation with thickness, so the mixed minerals can be fitted according to the empirical formula, and the results are shown in Table 4.

The independent variable x' in the table is the sample thickness, and the dependent variable y' was the peak gray value. The graphite and quartz were selected as pure and mixed minerals of 5.5 mm, and the gray values were 159.51 for graphite and 128.88 for quartz when $x = 5.5$ was brought into the regression equation of the low-energy region of pure minerals, and the value was 151.70 for graphite and quartz in the regression equation of the low-energy region of mixed minerals. This is consistent with the basic law of X-ray identification, which was verified for other samples. This indicates that the thickness of mixed minerals shows a good correlation with the gray value, and the correlation trend was the same for different mineral species.

3.3. Coal Samples. The coal samples of each density level of coking, gas, and fat coals were put into the feeding system separately, and the ash peaks of coal samples were obtained according to the pure mineral extraction ash peak method after processing the pictures by computer and plotted into ash peak curves as shown in Figure 6.

According to the ash value of coal samples, we can see that the ash value of different coals decreases gradually with the increase of density, and the ash value decreases gradually with the increase of thickness at the same density, which was consistent with the law of ash value of single minerals and mixed minerals. Upon further analysis, the model $y = a\cdot e^{bx}$ can be established for the ash value of different coal types at different densities versus coal particle size, and the regression models can be obtained for each of the above three coal samples. Among them, the decay model law of ash value of fat coal is shown in Figure 7.

From Figure 7, it can be seen that the ash values of fat coal samples show a correlation with the scale at the same density. The coking coal and gas coal also have the same pattern.

4. SUMMARY AND CONCLUSIONS

In this study, the test samples of single minerals, mixed minerals, and different coal ranks were prepared to study the variation law of the gray values of different mineral components at different thicknesses and densities, and the regression equations of the gray values of different minerals were fitted. The following conclusions were obtained:

(a) Four single-mineral and mixed-mineral test samples were imaged under X-ray irradiation, and the grayscale peak of each sample picture was extracted using MATLAB. The pattern between sample or thickness and grayscale was analyzed by regression analysis, and the pattern satisfied the empirical equation $y = a\cdot e^{bx}$.

(b) Bringing the independent variable thickness of 5.5 mm into the regression equation for mixed minerals and single minerals resulted in calculated coefficients of 159.51 and 128.88 for graphite and quartz, respectively, and 151.70 for graphite and quartz; this result corresponds to the density interval, and all other minerals conform to this rule, indicating that the gray variation is influenced by thickness and density.

(c) Three coal samples (coking, fat, and gas coals) of different thicknesses were selected by float and sink tests at each thickness with different densities. Their ash peaks were counted, and their thicknesses and densities showed significant patterns with respect to the ash values and tended to be consistent with the variation patterns of single minerals and mixed minerals.

■ AUTHOR INFORMATION

Corresponding Author

Jianqiang Yin — *School of Materials Science and Engineering, Anhui University of Science and Technology, 232001 Huainan, China;* ⊙ orcid.org/0000-0002-1383-2653; Email: a136439586@163.com

Authors

Chenguang Yang − *School of Materials Science and Engineering, Anhui University of Science and Technology, 232001 Huainan, China*

Liqin Wu − *School of Materials Science and Engineering, Anhui University of Science and Technology, 232001 Huainan, China*

Qiuyu Zeng − *School of Materials Science and Engineering, Anhui University of Science and Technology, 232001 Huainan, China*

Liwei Zhang − *School of Materials Science and Engineering, Anhui University of Science and Technology, 232001 Huainan, China*

Complete contact information is available at:
https://pubs.acs.org/10.1021/acsomega.2c05743

Notes

The authors declare no competing financial interest.

■ REFERENCES

(1) Wang, W.; Li, B.; Yao, X.; Lyu, J.; Ni, W. Air pollutant control and strategy in coal-fired power industry for promotion of China's emission reduction. *Front. Energy.* **2019**, *13*, 307−316.

(2) Wang, W.; Lyu, J.; Li, Z.; Zhang, H.; Yue, G.; Ni, W. Energy conservation in China's coal-fired power industry by installing advanced units and organized phasing out backward production. *Front. Energy.* **2019**, *13*, 798−807.

(3) O'Keefe, J. M.; Bechtel, A.; Christanis, K.; Dai, S.; DiMichele, W. A.; Eble, C. F.; Esterle, J. S.; Mastalerz, M.; Raymond, A. C.; Val entim, B.; Wagner, N.; Ward, C. R.; Hower, J. C. On the fundamental difference between coal rank and coal type. *Int. J. Coal. Geol.* **2013**, *118*, 58−87.

(4) Wu, X. F.; Chen, G. Q. Coal use embodied in globalized world economy: From source to sink through supply chain. *Renew. Sust. Energy Rev.* **2018**, *81*, 978−993.

(5) Li, D.; Wu, D.; Xu, F.; Lai, J.; Shao, L. Literature overview of Chinese research in the field of better coal utilization. *J. Clean. Prod.* **2018**, *185*, 959−980.

(6) Yang, J.; Chang, B.; Zhang, Y.; Zhang, Y.; Luo, W. PCViT: A Pre-Convolutional ViT Coal Gangue Identification Method. *Energies.* **2022**, *15*, 4189.

(7) Zhang, Q.; Wang, Z.; Zhang, J.; Jiang, H.; Wang, Y.; Yang, K.; Tian, X.; Yuan, L. Integrated green mining technology of "coal mining-gangue washing-backfilling-strata control-system monitoring"—taking Tangshan Mine as a case study. *Environ. Sci. Pollut. R.* **2022**, *29*, 5798−5811.

(8) Zhou, J.; Guo, Y.; Wang, S.; Cheng, G. Research on intelligent optimization separation technology of coal and gangue base on LS-FSVM by using a binary artificial sheep algorithm. *Fuel.* **2022**, *319*, 123837.

(9) Gao, R.; Sun, Z.; Li, W.; Pei, L.; Hu, Y.; Xiao, L. Automatic coal and gangue segmentation using u-net based fully convolutional networks. *Energies.* **2020**, *13*, 829.

(10) Singh, V.; Rao, S. M. Application of image processing and radial basis neural network techniques for ore sorting and ore classification. *Miner. Eng.* **2005**, *18*, 1412−1420.

(11) Li, L.; Wang, H.; An, L. Research on recognition of coal and gangue based on image processing. *World. J. Eng.* **2015**, *12*, 247−254.

(12) Alfarzaeai, M. S.; Niu, Q.; Zhao, J.; Eshaq, R. M. A.; Hu, E. Coal/gangue recognition using convolutional neural networks and thermal images. *IEEE Access.* **2020**, *8*, 76780−76789.

(13) Eshaq, R. M. A.; Hu, E.; Li, M.; Alfarzaeai, M. S. Separation between coal and gangue based on infrared radiation and visual extraction of the YCbCr color space. *IEEE Access.* **2020**, *8*, 55204−55220.

(14) Dou, D.; Zhou, D.; Yang, J.; Zhang, Y. Coal and gangue recognition under four operating conditions by using image analysis and Relief-SVM. *Int. J. Coal. Prep. Util.* **2020**, *40*, 473−482.

(15) Guo, Y.; Wang, X.; Wang, S.; Hu, K.; Wang, W. Identification method of coal and coal gangue based on dielectric characteristics. *IEEE Access.* **2021**, *9*, 9845−9854.

(16) Pu, Y.; Apel, D. B.; Szmigiel, A.; Chen, J. Image recognition of coal and coal gangue using a convolutional neural network and transfer learning. *Energies.* **2019**, *12*, 1735.

(17) Yin, J.; Zhu, H.; Zhu, J.; Zeng, Q.; Li, L.; Yang, C. Analyzing the identification mechanism of graphite and clay minerals in coal and gangue using X-rays. *Physicochem Probl. Mi.* **2021**, *58*, 24−36.

(18) Wang, X.; Wang, S.; Guo, Y.; Hu, K.; Wang, W. Dielectric and geometric feature extraction and recognition method of coal and gangue based on VMD-SVM. *Powder Technol.* **2021**, *392*, 241−250.

(19) Yang, J.; Peng, J.; Li, Y.; Xie, Q.; Wu, Q.; Wang, J. Gangue Localization and Volume Measurement Based on Adaptive Deep Feature Fusion and Surface Curvature Filter. *IEEE T Instrum Meas.* **2021**, *70*, 1−13.

(20) Zheng, K. H.; Gao, K. D.; Yang, Z. J.; Wang, Z. Y. Morphological characterization of crushed coal gangue by micro X-ray computed tomography scanning. *Int. J. Coal. Prep. Util.* **2022**, *42*, 1528−1547.

(21) Lin, C. L.; Miller, J. D. 3D characterization and analysis of particle shape using X-ray microtomography (XMT). *Powder Technol.* **2005**, *154*, 61−69.

(22) Jia, F.; Ramirez-Muñiz, K.; Song, S. Preparation and characterization of porous hematite through thermal decomposition of a goethite concentrate. *Min. Proc. Ext. Met. Rev.* **2014**, *35*, 193−201.

(23) Yuce, A. E. Grinding size estimation and beneficiation studies based on simple properties of ore components. *Physicochem Probl. Mi.* **2017**, *53*, 541−552.

(24) Zhao, Y.; Chen, L.; Yi, H.; Zhang, Y.; Song, S.; Bao, S. Vanadium transitions during roasting-leaching process of vanadium extraction from stone coal. *Minerals-Basel.* **2018**, *8*, 63.

(25) Chen, Y.; Xia, W.; Xie, G. Contact angle and induction time of air bubble on flat coal surface of different roughness. *Fuel* **2018**, *222*, 35−41.

(26) Kalha, C.; Fernando, N. K.; Bhatt, P.; Johansson, F. O.; Lindblad, A.; Rensmo, H.; Medina, L. Z.; Lindblad, R.; Siol, S.; Jeurgens, L. P.; Cancellieri, C.; Rossnagel, K.; Medjanik, K.; Schoenhense, G.; Simon, M.; Gray, A. X.; Nemšák, S.; Lömker, P.; Schlueter, C.; Regoutz, A. Hard x-ray photoelectron spectroscopy: a snapshot of the state-of-the-art in 2020. *J. Phys-Condens. Mater.* **2021**, *33*, 233001.

(27) Gades, L. M.; Cecil, T. W.; Divan, R.; Schmidt, D. R.; Ullom, J. N.; Madden, T. J.; Yan, D.; Miceli, A. Development of thick electroplated bismuth absorbers for large collection area hard X-ray transition edge sensors. *IEEE T. Appl. Supercon.* **2017**, *27*, 1−5.

(28) Schmidt, B.; Flohr, T. Principles and applications of dual source CT. *Phys. Medica.* **2020**, *79*, 36−46.

(29) Klassen, S. The photoelectric effect: Reconstructing the story for the physics classroom. *Sci. Educ.* **2011**, *20*, 719−731.

(30) Hajima, R.; Hayakawa, T.; Shizuma, T.; Angell, C. T.; Nagai, R.; Nishimori, N.; Sawamura, M.; Matsuba, S.; Kosuge, A.; Mori, M.; Seya, M. Application of Laser Compton Scattered gamma-ray beams to

nondestructive detection and assay of nuclear material. *Eur. Phys. J-Spec. Top.* **2014**, *223*, 1229−1236.

(31) Jacquet, M.; Bruni, C. Analytic expressions for the angular and the spectral fluxes at Compton X-ray sources. *J. Synchrotron Radiat.* **2017**, *24*, 312−322.

(32) Bartschat, K.; Brown, A.; Van der Hart, H. W.; Colgan, J.; Scott, N. S.; Tennyson, J. Computational treatment of electron and photon collisions with atoms, ions, and molecules: the legacy of Philip G Burke. *J. Phys. B-At. Mol. Opt.* **2020**, *53*, 192002.